In-vitro validation of inertial-sensor-to-bone alignment

Weygers, Ive; Kok, Manon; Seel, Thomas; Shah, Darshan; Taylan, Orçun; Scheys, Lennart; Hallez, Hans; Claeys, Kurt

DOI
10.1016/j.jbiomech.2021.110781

Publication date
2021

Document Version
Final published version

Published in
Journal of Biomechanics

Citation (APA)
Weygers, I., Kok, M., Seel, T., Shah, D., Taylan, O., Scheys, L., Hallez, H., & Claeys, K. (2021). In-vitro validation of inertial-sensor-to-bone alignment. *Journal of Biomechanics*, *128*, Article 110781. https://doi.org/10.1016/j.jbiomech.2021.110781

Journal of Biomechanics 128 (2021) 110781

Contents lists available at ScienceDirect

Journal of Biomechanics

journal homepage: www.elsevier.com/locate/jbiomech

In-vitro validation of inertial-sensor-to-bone alignment

Ive Weygers [a,*], Manon Kok [b], Thomas Seel [c], Darshan Shah [d], Orçun Taylan [d], Lennart Scheys [e,d], Hans Hallez [f], Kurt Claeys [a]

[a] KU Leuven campus Bruges, Department of Rehabilitation Sciences, 8200 Bruges, Belgium
[b] TU Delft, Department of Mechanical, Maritime and Materials Engineering, 2628 CD Delft, The Netherlands
[c] Friedrich-Alexander-Universität Erlangen-Nürnberg, Department Artificial Intelligence in Biomedical Engineering, 91054 Erlangen, Germany
[d] KU Leuven, Department of Development and Regeneration, Institute for Orthopaedic Research and Training (IORT), 3000 Leuven, Belgium
[e] University Hospitals Leuven, Division of Orthopaedics, 3000 Leuven, Belgium
[f] KU Leuven campus Bruges, Department of Computer Sciences, 8200 Bruges, Belgium

ARTICLE INFO

Keywords:
Sensor-to-segment alignment
Human movement analysis
IMU
Joint kinematics
Lower limb

ABSTRACT

A major shortcoming in kinematic estimation using skin-attached inertial sensors is the alignment of sensor-embedded and segment-embedded coordinate systems. Only a correct alignment results in clinically relevant kinematics. Model-based inertial-sensor-to-bone alignment methods relate inertial sensor measurements with a model of the joint. Therefore, they do not rely on properly executed calibration movements or a correct sensor placement. However, it is unknown how accurate such model-based methods align the sensor axes and the underlying segment-embedded axes, as defined by clinical definitions. Also, validation of the alignment models is challenging, since an optical motion capture ground truth can be prone to disturbances from soft tissue movement, orientation estimation and manual palpation errors. We present an anatomical tibiofemoral ground truth on an unloaded cadaveric measurement set-up that intrinsically overcomes these disturbances. Additionally, we validate existing model-based alignment strategies. Modeling the degrees of freedom leads to the identification of rotation axes. However, there is no reason why these axes would align with the segment-embedded axes. Relative inertial-sensor orientation information and rich arbitrary movements showed to aid in identifying the underlying joint axes. The first dominant sagittal rotation axis aligned sufficiently well with the underlying segment-embedded reference. The estimated axes that relate to secondary kinematics tend to deviate from the underlying segment-embedded axes as much as their expected range of motion around the axes. In order to interpret the secondary kinematics, the alignment model should more closely match the biomechanics of the joint.

1. Introduction

Human motion analysis is an extensively studied topic in biomechanics (Sankey et al., 2020). To understand the complexity in movement behaviors, researchers rely on laboratory equipment and computational methods for reconstructing in-silico joint kinematics (Camomilla et al., 2017). Currently, optical motion capture (OMC) is commonly used for tracking body movements via skin-attached reflective markers and infrared cameras (Weygers et al., 2020b). However, the required static laboratory environment for OMC limits practical applications and fuels the emerging trend toward alternative movement analysis methods using inertial measurement units (IMUs) (Picerno, 2017). Body movements are estimated from the measurements of skin-attached IMUs, involving complex computational sensor fusion steps to optimally combine the different information sources (Kok et al., 2017; Laidig et al., 2017). While there is an increasing interest in inertial sensor-based joint kinematic estimation in clinical applications, it is a notorious problem that only after a correct alignment of the inertial sensor axes with the underlying segment-embedded axes (that are defined by the clinical definitions (Grood and Suntay, 1983; Wu et al., 2002), clinically relevant kinematics can be obtained. Since OMC-based methods directly relate to anatomical landmarks via manually palpated positions of reflective markers, standards are formed for the alignment procedure and reporting of joint kinematics (Davis et al., 1991; Vanrenterghem et al., 2010). In IMU-based kinematic analysis, currently, a wide variety of inertial-sensor-to-bone alignment methods exist (Pacher et al., 2020; Vitali and Perkins, 2020). Furthermore, IMU-based alignment methods are most often validated by means of their resulting joint kinematics, with respect to an OMC-based ground

* Corresponding author.
E-mail address: ive.weygers@kuleuven.be (I. Weygers).

https://doi.org/10.1016/j.jbiomech.2021.110781
Accepted 27 September 2021
Available online 2 October 2021

truth (Seel et al., 2012; Luinge et al., 2007; Tadano et al., 2013; McGrath and Stirling, 2020). This raises two major concerns: First, the validation of inertial-sensor-to-bone alignment by means of kinematics makes it difficult to differentiate between errors that originate from inertial sensor orientation estimation and errors that stem from kinematic cross-talk due to mis-alignments. Second, it has been concluded that skin movement, especially at the thigh is so prominent that one might question the use of an OMC as a Ref. Reinschmidt et al. (1997), Freeman and Pinskerova (2005) and Hull (2020).

Vitali and Perkins (2020) reviewed the variety in inertial sensor-to-bone alignment methods and states that a great majority of IMU-based kinematic studies assume that the sensing axes of the skin-attached IMUs approximately align with the underlying segment-embedded (Bouvier et al., 2015) reference system (Dejnabadi et al., 2005; Djurić-Jovičić et al., 2011). However, violations against such assumptions naturally yield kinematic cross-talk errors when movements in multiple movement planes are of interest (Hull, 2020; Freeman and Pinskerova, 2005). In the case of an arbitrary joint with no restrictions on the rotational degrees of freedom (DoF) and rigid proximal and distal attached segments, it is crucial to determine at least the direction of two body-fixed rotation axes, that do not need to be orthogonal and relate with anatomical landmarks, to report clinically relevant kinematics (Hollister et al., 1993). For the tibiofemoral (TF) joint movement, this translates into identifying the direction of the femur-fixed flexion axis and a tibia-fixed rotation axis as seen from the attached inertial sensors. To obtain these axes, also functional approaches have been proposed, where limbs are sequentially rotated around isolated axes following a set of known calibration movements and postures (Luinge et al., 2007; Tadano et al., 2013; Chardonnens et al., 2013). Although such functional sensor-to-bone alignment methods are easy to conduct, their accuracy highly depends on the ability of the subject or instructor to execute movements around designated and assumed isolated axes. Moreover, Picerno et al. (2008, 2019) utilized auxiliary equipment for the identification of anatomical landmarks that are used to define joint axes within the sensor-embedded coordinate systems.

Recently, model-based approaches are gaining interest (Seel et al., 2012; Olsson et al., 2019; Müller et al., 2017; McGrath and Stirling, 2020) and focus on relating inertial measurements with the underlying segment-embedded reference system, without making any assumption on sensor placement or calibration movements. Seel et al. (2012) first proposed a model-based inertial-sensor-to-bone alignment method that exploits the kinematic constraints induced by the joint to estimate a functional hinge joint axis from gyroscope measurements using an optimization-based algorithm. For two degrees-of-freedom (DoF) joints, Müller et al. (2017) proposed a method that exploits an elbow joint model to estimate two dominant body-fixed joint axes from gyroscope measurements and relative sensor orientation estimates. Norden et al. (2018) extended this intuition for three-dimensional joints to estimate the body-fixed underlying axes for the hip and knee joint. None of these novel model-based methods have been validated with respect to a real ground truth and it remains unclear how accurate they can relate the sensor's axes with the underlying segment-embedded reference system.

In this study we present a true anatomical reference for inertial-sensor-to-bone alignment methods, from dynamic motions on an unloaded cadaver. The validation method overcomes error sources that are common in an OMC, e.g., disturbances from soft tissue artifacts (STA) (Freeman and Pinskerova, 2005), sensor orientation estimation errors (Kok et al., 2017) and manual palpation errors (Schwartz et al., 2004), while overcoming the ethical difficulties for an in vivo measurement protocol, e.g., Lafortune et al. (1992). We focus on the TF joint, which is most studied for inertial-sensor-to-bone alignment (Vitali and Perkins, 2020). Additionally, we validate and critically reflect on model-based inertial-sensor-to-bone alignment strategies for the identification of underlying segment-embedded joint axes, with the proposed reference.

2. Methods

2.1. Experimental set-up

Following ethical approval by the institutional board (HN09) a complete fresh frozen cadaveric lower limb (F, left, 52 yrs, no knee injuries) disarticulated at the level of the hip was imaged using computed tomography (CT) with retro-reflective marker clusters (attached on bone-pins) for the femur and tibia (Fig. 1) to construct a three-dimensional (3D) surface of both segments in Mimics (Materialise, Leuven, Belgium). Each bone-pin was equipped with a rigidly attached IMU (Mtw Awinda, Xsens, Enschede, the Netherlands). A hardware time synchronization was used to simultaneously capture optical marker trajectories by a six-camera OMC set-up (MX+, Vicon, Oxford, UK) and measurement data of the IMUs, with a sample rate of 100 Hz.

2.2. Measurement protocol

Experienced physiotherapists performed unloaded motions of the knee joint for 30 s for each of the following varying protocol variables, in all possible combinations: 3 movement plane options, 3 movement excitation options and 2 levels of tibiofemoral flexion range of motion (RoM) (total of N=18 trials). We differentiated between movements in a

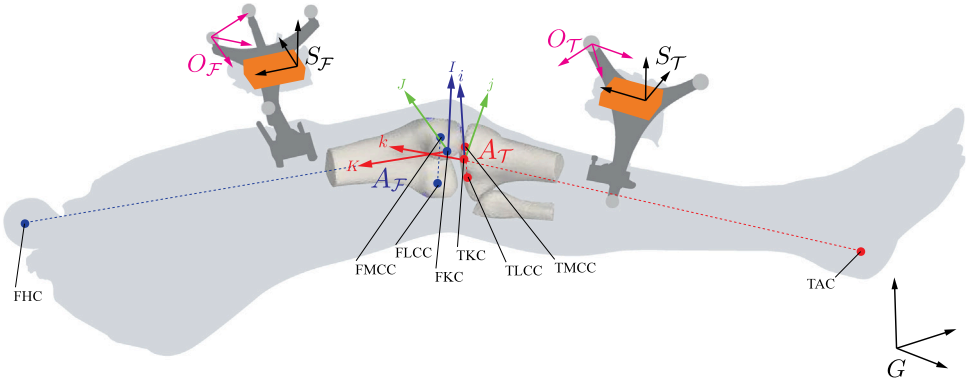

Fig. 1. Experimental set-up: A cadaveric lower limb in a horizontal position with rigidly attached bone-pins on the femur ($_\mathcal{F}$) and tibia ($_\mathcal{T}$) segments. Each bone-pin is equipped with retro-reflective marker clusters that form optical coordinate systems $O_\mathcal{F}$ and $O_\mathcal{T}$ and inertial sensors with sensor coordinate systems $S_\mathcal{F}$ and $S_\mathcal{T}$. Anatomical reference coordinate systems $A_\mathcal{F}$ and $A_\mathcal{T}$ are defined on the base of virtual anatomical landmarks (FMCC: femoral medial condyle center, FLCC: femoral lateral condyle center, FKC: femoral knee center, FHC: femoral hip center, TMCC: tibial medial condyle center, TLCC: tibial lateral condyle center, TKC: tibial knee center, TAC: tibial ankle center) on the 3D-surface bone models, illustrated as dots for femur (blue) and tibia (red). All coordinate frames can be tracked with respect to an OMC references coordinate system G, after the necessary coordinate frame transformations. (For interpretation of the references to color in this figure legend, the reader is referred to the web version of this article.)

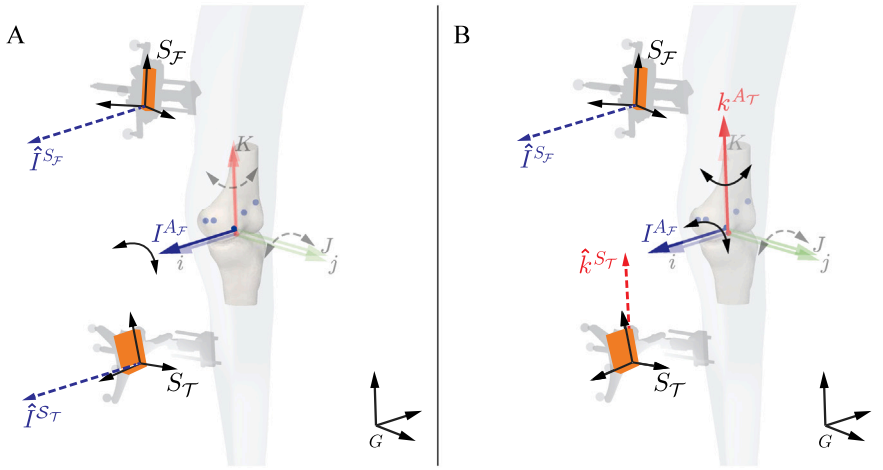

Fig. 2. Two model-based inertial-sensor-to-bone alignment strategies; (A) Hinge joint model: interest lies in estimating the direction of a common femur-attached flexion-axis I^{A_F} in sensor coordinate systems S_F and S_T, (B) Two-dominant-axes model: interest lies in estimating two body-fixed axes directions I^{A_F}, k^{A_T} in respectively sensor coordinate systems S_F and S_T.

fixed vertical movement plane (specimen was placed in a position with a horizontal femoral flexion-axis), fixed horizontal movement plane (specimen was placed in a position with a vertical femoral flexion-axis) and a mixed movement plane that can change its orientation over time. Movement excitation was quantified after execution of the experiments as slow (norm angular velocity 0.73±0.51 rad/s (femur-attached inertial sensor) 0.62 ± 0.53 rad/s (tibia-attached inertial sensor)), fast (norm angular velocity 1.55±1.09 rad/s (femur-attached inertial sensor) 1.51± 1.28 rad/s (tibia-attached inertial sensor)) and mixed as a random sequence of slow and fast movement periods. Two RoMs – 60 degrees to replicate normal gait and 110 degrees to replicate squatting (Freeman and Pinskerova, 2005) – were accurately executed with the aid of a custom script for realtime feedback on TF flexion.

2.3. Anatomical reference & coordinate system definitions

Anatomical landmarks were located on the 3D-surface bone models with Mimics for the femur and tibia. The landmarks were transformed from a CT-scan reference coordinate system to the OMC reference coordinate system G. Transformation matrices were denoted by O and defined on the base of three non-collinear pin-attached optical markers that were identified in both the CT-scan and the OMC reference coordinate systems. This resulted in virtual anatomical landmarks within the OMC reference coordinate system that are used to represent a true anatomical segment-embedded coordinate system A (Grood and Suntay, 1983). Furthermore, S denotes an inertial sensor coordinate system in which inertial measurements are sensed and joint axes are estimated. We differentiate between femur ($_F$) and tibia ($_T$) segments and will use the notation $\hat{v}^{A_F}$ to represent an estimate of a vector v, expressed in anatomical femur (A_F) coordinates.

2.4. Inertial-sensor-to-bone alignment: hinge joint model

Seel et al. (2012) first proposed the general hinge joint model and applied it to the TF joint: a system with two segments that are connected by a hinge joint is considered as depicted in Fig. 2A. Both segments are equipped with rigidly attached and arbitrarily oriented inertial sensors S_F and S_T. Following Nowka et al. (2019) and since by definition $I^{S_T} = \mathbf{R}_t^{S_T S_F} I^{S_F}$, the hinge joint movement can be modeled by a kinematic constraint as

$$\omega_t^{S_T} - \left(I^{S_T}\right)^{\mathrm{T}} \omega_t^{S_T} I^{S_T} = \mathbf{R}_t^{S_T S_F} \omega_t^{S_F} - \left(I^{S_T}\right)^{\mathrm{T}} \left(\mathbf{R}_t^{S_T S_F} \omega_t^{S_F}\right) I^{S_T}, \tag{1}$$

where ω_t defines the measured and time-varying ($_t$) angular velocity, the $^{\mathrm{T}}$ operator denotes a transpose operation. Here, the hinge joint axis I needs to be estimated in each sensor coordinate system: I^{S_F}, I^{S_T}. If an accurate estimate of the relative sensor orientation $\mathbf{R}_t^{S_T S_F}$ is not available, (1) can be reformulated following Seel et al. (2012) as

$$e_{\text{hinge}} = \left\| \omega_t^{S_T} \times I^{S_T} \right\|_2 - \left\| \omega_t^{S_F} \times I^{S_F} \right\|_2, \tag{2}$$

where $\times$ denotes the cross-product operation. Alternatively, if an accurate estimate of the relative sensor orientation $\mathbf{R}_t^{S_T S_F}$ can be obtained (in the present study $\mathbf{R}_t^{S_T S_F}$ is obtained from the optical marker clusters in the presented experimental set-up from Section 2.1), (1) may be reformulated (Appendix) in a difference of vectors rather than scalars as,

$$e_{\text{hinge}} = \left(\omega_t^{S_T} \times I^{S_T}\right) - \mathbf{R}_t^{S_T S_F} \left(\omega_t^{S_F} \times I^{S_F}\right). \tag{3}$$

Intuitively (2) and (3) imply that the relative motion between the sensors are confined to be around a common joint axis $I^G = \mathbf{R}^{GS_F} I^{S_F} = \mathbf{R}^{GS_T} I^{S_T}$. All other angular velocities should be sensed in the same way in both connecting sensors. Solutions for I^{S_F} and I^{S_T} can be found in a Gauss–Newton approach (Nocedal and Wright, 2006) by minimizing (2) or (3) as further described in Seel et al. (2012).

2.5. Inertial-sensor-to-bone alignment: two-dominant-axes model

Besides a dominant sagittal movement, the TF joint also naturally permits motions in secondary movement planes with rotations around a tibia-fixed axis k^{S_T} and ab/adduction movements around a floating axis j perpendicular to the two axes I^{S_F} and k^{S_T} (Iwaki et al., 2000). These secondary kinematics violate the general hinge joint model in (2) and (3), that expect the TF joint to rotate only about one primary axis. Norden et al. (2018) proposed an iterative approach to estimate two segment-fixed rotation axes I^{S_F}, k^{S_T} (and a resulting perpendicular third axis J^{S_F}) by considering the relative joint angular velocity $\omega_{r,t}$ as a combination of rotations around the three axes, as

$$\omega_{r,t}^{S_F} = \alpha_t I^{S_F} + \beta_t J^{S_F} + \gamma_t \mathbf{R}_t^{S_F S_T} k^{S_T}, \tag{4}$$

with $\omega_{r,t}^{S_F}$ the relative angular velocity that can be computed as $\omega_{r,t}^{S_F} = -\omega_t^{S_F} + \mathbf{R}_t^{S_F S_T} \omega_t^{S_T}$, which excludes all common angular velocities in the connecting IMUs. In order to estimate two dominant segment-fixed rotation axes I^{S_F} and k^{S_T} as illustrated in Fig. 2B, Norden et al. (2018) impose the restriction that the relative angular velocity when expressed in the femur-attached sensor ($\omega_{r,t}^{S_F}$) must be dominantly around I^{S_F} and that the remaining relative angular velocity, expressed in the tibia-attached sensor shall be around k^{S_T}. The remaining angular velocity is obtained after removing rotations around the first dominant axis

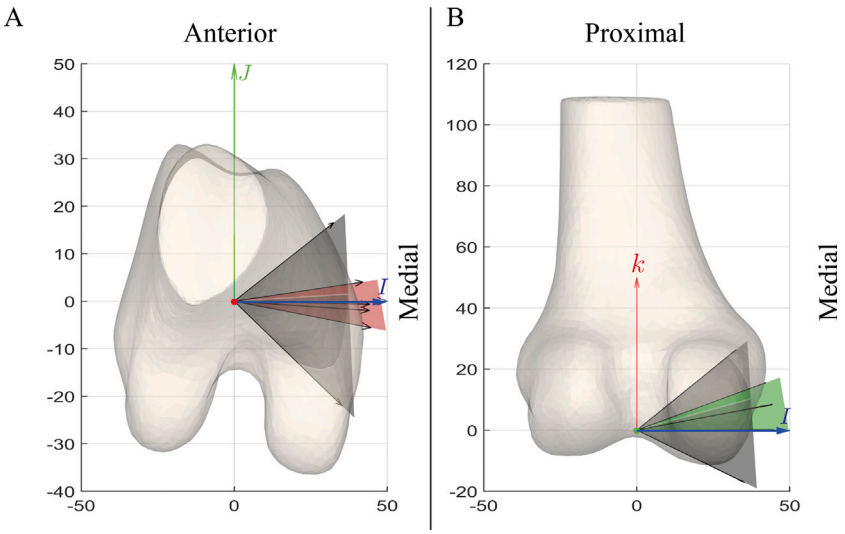

Fig. 3. Experimental results for the hinge joint strategy for all trials, in gray for model implementation (2) and in color for model implementation (3): mean estimated femur-fixed joint axis $\overline{\hat{I}^{A_F}}$ with $\pm SD$ bounds projected on the femur transverse (A) and frontal (B) movement planes. (For interpretation of the references to color in this figure legend, the reader is referred to the web version of this article.)

as $\omega_{r,t}^{S_T} = \omega_{r,t}^{S_T} - \left(I_t^{S_T}\right)^{\mathrm{T}} \omega_{r,t}^{S_T} I_t^{S_T}$. Note that the second dominant axis depends on the first dominant axis and that $\mathbf{R}_t^{S_F S_T}$ is in (4) assumed to be available. Both axes are iteratively (every 21 samples) updated from averaged, normalized and low-pass filtered relative angular velocities in their corresponding sensor coordinate systems, as further described in Norden et al. (2018).

2.6. Data processing & assessment

The models and tools for processing and assessment of the data were implemented in a custom Matlab (R2019b, Mathworks, Natick, USA) script. The proposed experimental set-up allows for an evaluation of the IMU-based estimates of the underlying segment-embedded joint axes $\hat{v}^S$. We express $\hat{v}^S$ in the underlying segment-embedded reference system ($\hat{v}^A$) and compare against the truth (v^A), after applying the necessary consecutive rotations:

$$\hat{v}^A = \mathbf{R}_t^{AO} \mathbf{R}^{OS} \hat{v}^S, \tag{5}$$

where a constant misalignment between inertial sensing frame and optical markers $\mathbf{R}^{OS}$ is obtained, for each IMU, from the closed-form solution in Theorem 4.1 from Hol (2011) by using all experimental data points, to cover most of the rotation space, as concluded by Chardonnens et al. (2012). $\mathbf{R}_t^{AO}$ represents the rotation between the coordinate system on the base of three non-collinear pin-attached optical markers and a segment-embedded reference system. Note that a rigidly attached inertial sensor implies that (5) can be applied to any time point. Since both model-based strategies from Sections 2.4 and 2.5 do not require explicit knowledge on the limb side, direction errors were corrected by inverting the estimated axes as $\hat{v}^A = -\hat{v}^A$. We furthermore overcome introducing errors from IMU orientation estimation by using $\mathbf{R}_t^{S_F S_T}$ that was obtained from the optical marker clusters (Fig. 1) after alignment with the inertial sensor axes.

The proposed validation method allows for a decomposition of the angular error of the estimated axes in two anatomical planes: For example, the estimated femur-fixed flexion-axis $\hat{I}^{S_F}$ can be projected onto the transverse (with K^A as the normal) and frontal (with J^A as the normal) femur anatomical plane. For each of the 18 trials, four consecutive time windows (500 samples each) of the experimental inertial measurements were processed with the alignment strategies from Sections 2.4 and 2.5 to obtain 72 windows.

2.7. Statistical analysis

The obtained angular errors of the estimated axes were tested on normality (Shapiro–Wilk test). Since the data was not normally distributed, differences in the absolute errors between anatomical movement planes and estimated axes were analyzed using Mann–Whitney U test. Kruskal–Wallis test and Brown–Forsythe's post hoc test were used to test for significant differences between varying parameters in the measurement protocol. All statistical analyses were performed using SPSS Statistics v27 (SPSS Inc., Chicago, IL, USA). Significance is accepted if $p < 0.05$.

3. Results

When considering hinge joint kinematics, which was discussed in Section 2.4, the estimated position of the underlying femur-fixed axis $\hat{I}^{A_F}$ in the implementation (2) deviated significantly more ($p < 0.001$) from the truth (26.07° ± 20.74°) than the estimates in implementation (3) (8.58° ± 7.86°). With respect to (3), the estimated position of the underlying femur-fixed axis $\hat{I}^{A_F}$ deviated significantly more ($p < 0.001$) from the truth in the frontal movement plane (with absolute errors 12.20° ± 9.06°) than in the transverse movement plane (4.95° ± 3.95°), regardless of the measurement protocol parameters (Fig. 3). No significant differences were found by altering the RoM or movement excitation (Fig. 4). Significantly lower ($p < 0.001$) errors were obtained in the transverse femur plane (2.27° ± 1.61°) when the movement plane was not fixed in a vertical (7.34° ± 5.17°) or horizontal (5.25° ± 2.29°) position. The estimated femur-fixed axis deviated significantly more ($p < 0.001$) in frontal femur plane, when the system was moved in a horizontal position (19.25° ± 10.22°), when compared to a vertical (9.03° ± 5.91°) or changing position (8.31° ± 6.02°).

When considering two dominant rotation axes, which was discussed in Section 2.5, the estimated position of the tibia-fixed axis $\hat{k}^{A_T}$ deviated significantly more ($p < 0.001$) from the true position (10.52° ± 7.22°) than the estimated position of the femur-fixed axis $\hat{I}^{A_F}$ (5.45° ± 2.86°) regardless of the measurement protocol parameters (Fig. 5). The estimated femur-fixed flexion axis $\hat{I}^{A_F}$ deviated significantly ($p < 0.001$) more from the truth in frontal plane (7.42° ± 2.72°) than in transverse plane (3.48°±1.10°). No significant differences were found by altering the movement excitation. Estimates that were obtained during TF flexion RoM equal to 110° were significantly lower ($p < 0.001$) in frontal plane for both femur-fixed (RoM=60: 8.57° ± 2.65°, RoM=110:

6.28° ± 2.29°) and tibia-fixed (RoM=60: 9.76° ± 2.21°, RoM=110: 7.04° ± 1.22°) axes. A significant decrease in errors is visible in Fig. 6 for the sagittal tibia plane and frontal femur plane, together with a slightly increasing femur transverse plane error, when the movement plane could change over time.

4. Discussion

To the best of our knowledge, this is the first study that presents a validation method for the assessment of inertial-sensor-to-bone alignment against a true anatomical reference. Evaluation of sensor-misalignment is done in anatomical planes to explain error sources that would otherwise be hidden in kinematic cross-talk errors (Hull, 2020; Freeman and Pinskerova, 2005). The validation method overcomes the limitations of an OMC reference that can be affected by:

1. Disturbances from STA, (while evaluating the biological TF biomechanical system Freeman and Pinskerova, 2005), by rigidly attaching IMUs on the bones of a cadaveric specimen.
2. Sensor orientation estimation errors (Kok et al., 2017), by making use of accurate trajectories of optical marker clusters.
3. Manual palpation errors of anatomical landmarks (Schwartz et al., 2004), by accurate identification of landmarks on 3D surface models from CT-scanning (Victor et al., 2009).

Model-based inertial-sensor-to-bone alignment methods overcome sensor placement assumptions, calibration procedures and auxiliary equipment (Picerno et al., 2008, 2019; van den Noort et al., 2014). The unknown relation between sensor axes and the underlying segment-embedded joint axes is obtained by relating a model of the joint biomechanics with inertial measurements and/or relative sensor orientation estimates. Therefore, a direct connection with the underlying segment-embedded reference system is missing. When TF joint movement is simplified to hinge joint mechanics, the inclusion of relative orientation information within the model (3) seems to help overcoming influences of violations to the hinge model assumption. But at the price of having to know and rely on IMU-based orientation estimates.

A two-dominant axes strategy as in Norden et al. (2018) most closely relates with the clinical definitions for describing the relative movement of the underlying segment-embedded reference system (Grood and Suntay, 1983; Wu et al., 2002). The dependency of a second-dominant axis on a first-dominant axis might explain the iterative implementation choice, but a globally unique optimal solution cannot be guaranteed. This might explain the higher error ranges that were obtained for the tibia-fixed axis. A possible future extension might benefit from the magnitude of the residual relative angular velocities (after removing movement about a primary axis of rotation) to exclude potential outliers that do not contain information about the identification of a secondary tibia-fixed rotation axis. In the same line of interest would be the identification of the (non)linearity of the coupling between flexion and rotations about secondary axes (and validation with the presented reference) to acquire subject-specific insight about, e.g., movement adaptations (Zeng et al., 2017), ligament strength (Wada et al., 2017). The estimates of the femur-fixed axes predominantly lie in the first quadrant (Fig. 5). This may relate with the direction of the mechanical femur flexion axis, after backward rolling of the femur (Iwaki et al., 2000) during flexion. Moreover, the estimates of the first dominant femur-fixed axis aligned significantly better with the truth than the tibia-fixed axis. This might be explained by the limited resulting amplitudes in the relative angular velocity after removing dominating rotations around the first-dominant flexion axis. This is furthermore in line with the slightly better results that were obtained for larger RoM. The femur-fixed axis estimates were more sensitive to the movement planes than the tibia-fixed axis estimates, which relates to the known conditions of identifiability for the hinge joint model (Nowka et al., 2019). The greater deviation in sagittal

Fig. 4. Absolute errors with SD for model implementation (3) and the influences of the different measurement protocol parameters on the estimation results.

movement plane for the estimated position of the tibia-fixed axis can be expected, since no explicit knowledge within the applied model on its

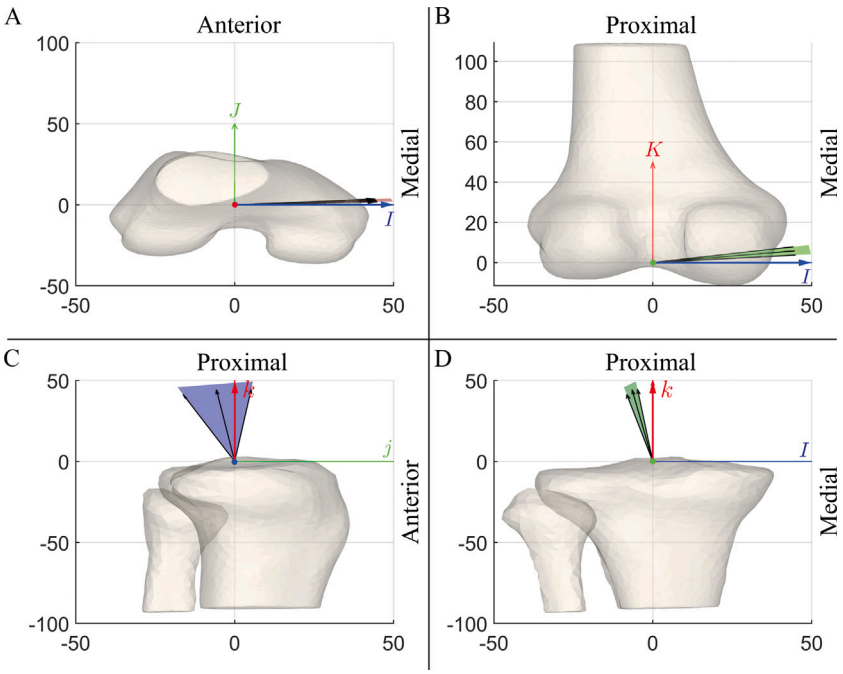

Fig. 5. Experimental results for the two-dominant-axes strategy for all trials: Mean estimated femur-fixed joint axis $\overline{\hat{I}^{A_F}}$ with $\pm SD$ bounds projected on the transverse (A) and frontal (B) movement planes and mean estimated tibia-fixed $\overline{\hat{k}^{A_T}}$ joint axis with $\pm SD$ bounds projected on the sagittal (C) and frontal (D) movement planes.

exact position is given. McGrath and Stirling (2020) recently proposed a method to restrict solutions in this plane, by minimizing the angular distance between the tibia rotation axis and a line connecting the joint centers of the proximal and distal joints (which can be estimated with high accuracy using inertial sensors Crabolu et al., 2017), to lie in anthropometric ranges identified by Hollister et al. (1993). However, they do not report on the precise effect of including this information.

The experiment was applied to only one specimen and can be considered a case-study. However, multiple repetitions of the same movement strengthens the obtained results. This in-vitro experimental set-up is unable to include natural contraction of muscles and resulting STA that arise in an in-vivo measurement set-up. However, unloaded motions on cadavers are often used to describe the relative movement of the bones (Iwaki et al., 2000; Pinskerova et al., 2004; Wilson et al., 2000). The proposed anatomical reference can be prone to misalignment errors between inertial sensor and optical marker-based coordinate systems (Hol, 2011). Small (< 1°) errors were reported for a similar method (Lee and Jung, 2018). As such, the implications of this on our outcomes are likely to be only minimal.

In conclusion, while inertial sensors are receiving increasing interest on orientation estimation for clinical applications (Laidig et al., 2017; Kok et al., 2017; Weygers et al., 2020a), only after a correct inertial-sensor-to-bone alignment, clinically relevant comparable kinematics can be obtained. Modeling the degrees of freedom of the joint does not seem to result in an identification of axes that align with underlying segment-embedded reference system (Grood and Suntay, 1983). With respect to the tibiofemoral joint, large ranges of motion in sagittal movement plane and rich arbitrary movements aid in identifying a first dominant axis sufficiently well to obtain sagittal kinematics. The estimated rotational joint axes that relates to secondary kinematics tend to deviate from the segment-embedded axes as much as the expected range of motion around the axes (even in the artificial cadaver study that excludes common error sources) (Iwaki et al., 2000). A further decomposition of the relative movements around these secondary axes will not result in comparable kinematics with the validated alignment strategies. In order to interpret the secondary kinematics, the inertial-sensor-to-bone alignment model should more closely match the biomechanics of the joint (Dzialo et al., 2018).

Declaration of competing interest

The authors declare that they have no known competing financial interests or personal relationships that could have appeared to influence the work reported in this paper.

Acknowledgments

The authors wish to thank Elias Theunynck and Emiel Nieuwlaet for their assistance during data collection. This work was supported by the European Regional Development Fund – We-lab for HTM [number 1047].

Appendix. Including rotation information in the hinge joint model

In Section 2.4 we presented formulation (3) which can be derived from (1) as

$$\begin{aligned}
\omega_t^{S_T} - (I^{S_T})^{\mathrm{T}}\omega_t^{S_T} I^{S_T} &= \mathbf{R}_t^{S_T S_F}\omega_t^{S_F} - (I^{S_T})^{\mathrm{T}}(\mathbf{R}_t^{S_T S_F}\omega_t^{S_F}) I^{S_T} \\
I^{S_T} \times \left(\omega_t^{S_T} - (I^{S_T})^{\mathrm{T}}\omega_t^{S_T} I^{S_T}\right) &= I^{S_T} \times \left(\mathbf{R}_t^{S_T S_F}\omega_t^{S_F} - (I^{S_T})^{\mathrm{T}} \right. \\
&\quad \left. \times (\mathbf{R}_t^{S_T S_F}\omega_t^{S_F}) I^{S_T}\right) \\
\left(I^{S_T} \times \omega_t^{S_T}\right) - \left(I^{S_T} \times \left((I^{S_T})^{\mathrm{T}}\omega_t^{S_T} I^{S_T}\right)\right) &= \left(I^{S_T} \times \left(\mathbf{R}_t^{S_T S_F}\omega_t^{S_F}\right)\right) \\
&\quad - \left(I^{S_T} \times \left((I^{S_T})^{\mathrm{T}}(\mathbf{R}_t^{S_T S_F}\omega_t^{S_F}) I^{S_T}\right)\right),
\end{aligned}$$

since for any vector $\mathcal{V}$, $\left(I^{S_T} \times (I^{S_T})^{\mathrm{T}} \mathcal{V} I^{S_T}\right) = \begin{bmatrix} 0 & 0 & 0 \end{bmatrix}^{\mathrm{T}}$ and $I^{S_T} = \mathbf{R}_t^{S_T S_F} I^{S_F}$, it follows that

$$\begin{aligned}
\omega_t^{S_T} \times I^{S_T} &= \left(\mathbf{R}_t^{S_T S_F}\omega_t^{S_F} \times \mathbf{R}_t^{S_T S_F} I^{S_F}\right) \\
\omega_t^{S_T} \times I^{S_T} &= \mathbf{R}_t^{S_T S_F}\left(\omega_t^{S_F} \times I^{S_F}\right).
\end{aligned}$$

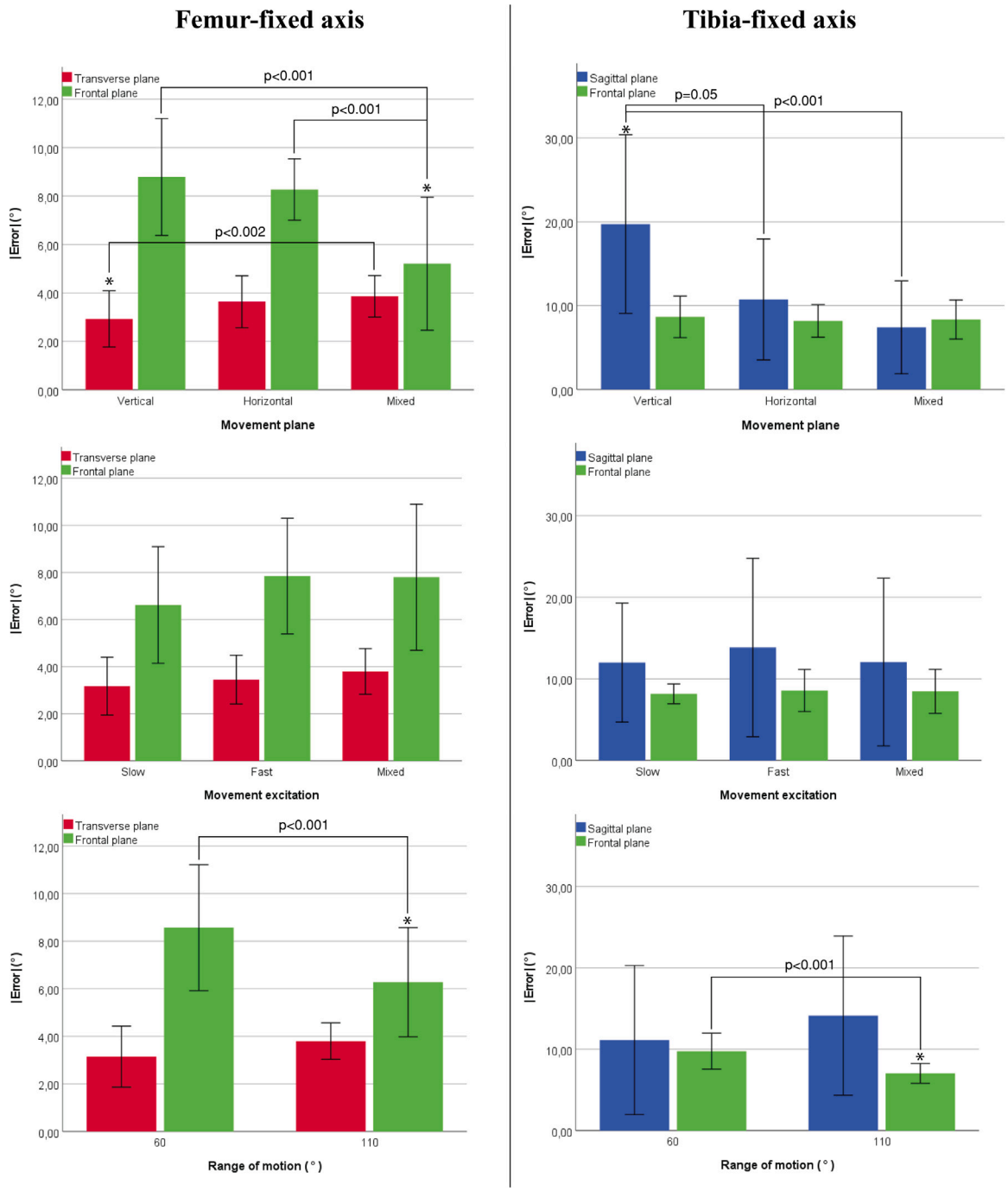

Fig. 6. Absolute errors with SD for the inertial-sensor-to-bone alignment two-dominant-axes model implementation and the influences of the different measurement protocol parameters on the estimation results.

References

Bouvier, B., Duprey, S., Claudon, L., Dumas, R., Savescu, A., 2015. Upper limb kinematics using inertial and magnetic sensors: Comparison of sensor-to-segment calibrations. Sensors 15 (8), 18813–18833.

Camomilla, V., Cappozzo, A., Vannozzi, G., 2017. Three-dimensional reconstruction of the human skeleton in motion. In: Müller, B., Wolf, S.I., Brueggemann, G.-P., Deng, Z., McIntosh, A., Miller, F., Selbie, W.S. (Eds.), Handbook of Human Motion. Springer International Publishing, Cham, pp. 1–29.

Chardonnens, J., Favre, J., Aminian, K., 2012. An effortless procedure to align the local frame of an inertial measurement unit to the local frame of another motion capture system. J. Biomech. 45 (13), 2297–2300.

Chardonnens, J., Favre, J., Cuendet, F., Gremion, G., Aminian, K., 2013. A system to measure the kinematics during the entire ski jump sequence using inertial sensors. J. Biomech. 46 (1), 56–62.

Crabolu, M., Pani, D., Raffo, L., Conti, M., Crivelli, P., Cereatti, A., 2017. In vivo estimation of the shoulder joint center of rotation using magneto-inertial sensors: MRI-based accuracy and repeatability assessment. Biomed. Eng. Online 16 (1), 34.

Davis, R.B., Ounpuu, S.., Tyburski, D., Gage, J.R., 1991. A gait analysis data collection and reduction technique. Hum. Mov. Sci. 10 (5), 575–587.

Dejnabadi, H., Jolles, B.M., Aminian, K., 2005. A new approach to accurate measurement of uniaxial joint angles based on a combination of accelerometers and gyroscopes. IEEE Trans. Biomed. Eng. 52 (8), 1478–1484.

Djurić-Jovičić, M.D., Jovičić, N.S., Popović, D.B., 2011. Kinematics of gait: New method for angle estimation based on accelerometers. Sensors 11 (11), 10571–10585.

Dzialo, C., Pedersen, P., Simonsen, C., Jensen, K., de Zee, M., Andersen, M., 2018. Development and validation of a subject-specific moving-axis tibiofemoral joint model using MRI and EOS imaging during a quasi-static lunge. J. Biomech. 72, 71–80.

Freeman, M., Pinskerova, V., 2005. The movement of the normal tibio-femoral joint. J. Biomech. 38 (2), 197–208.
Grood, E.S., Suntay, W.J., 1983. A joint coordinate system for the clinical description of three-dimensional motions: Application to the knee. J. Biomech. Eng. 105 (2), 136–144.
Hol, J.D., 2011. Sensor Fusion and Calibration of Inertial Sensors, Vision, Ultra-Wideband and GPS (Ph.D. thesis). Dept. Elect. Eng. Autom. Control, Linköping Univ., Linköping, Sweden.
Hollister, A.M., Jatana, S., Singh, A.K., Sullivan, W.W., Lupichuk, A.G., 1993. The axes of rotation of the knee.. Clin. Orthop. Relat. Res. (1976-2007) 290, 259–268.
Hull, M.L., 2020. Coordinate system requirements to determine motions of the tibiofemoral joint free from kinematic crosstalk errors. J. Biomech. 109, 109928.
Iwaki, H., Pinskerova, V., Freeman, M.A., 2000. Tibiofemoral movement 1: the shapes and relative movements of the femur and tibia in the unloaded cadaver knee. J. Bone Joint Surg. Br. Vol. 82 (8), 1189–1195.
Kok, M., Hol, J.D., Schön, T.B., 2017. Using Inertial Sensors for Position and Orientation Estimation.
Lafortune, M., Cavanagh, P., Sommer, H., Kalenak, A., 1992. Three-dimensional kinematics of the human knee during walking. J. Biomech. 25 (4), 347–357.
Laidig, D., Schauer, T., Seel, T., 2017. Exploiting kinematic constraints to compensate magnetic disturbances when calculating joint angles of approximate hinge joints from orientation estimates of inertial sensors. In: 2017 International Conference on Rehabilitation Robotics (ICORR). pp. 971–976.
Lee, J.K., Jung, W.C., 2018. Quaternion-based local frame alignment between an inertial measurement unit and a motion capture system. Sensors 18 (11).
Luinge, H., Veltink, P., Baten, C., 2007. Ambulatory measurement of arm orientation. J. Biomech. 40 (1), 78–85.
McGrath, T., Stirling, L., 2020. Body-worn IMU human skeletal pose estimation using a factor graph-based optimization framework. Sensors 20 (23).
Müller, P., Bégin, M., Schauer, T., Seel, T., 2017. Alignment-free, self-calibrating elbow angles measurement using inertial sensors. IEEE J. Biomed. Health Inf. 21 (2), 312–319.
Nocedal, J., Wright, S., 2006. Numerical Optimization. Springer Series in Operations Research.
van den Noort, J.C., Wiertsema, S.H., Hekman, K.M., Schönhuth, C.P., Dekker, J., Harlaar, J., 2014. Reliability and precision of 3D wireless measurement of scapular kinematics. Med. Biol. Eng. Comput. 52 (11), 921–931.
Norden, M., Müller, P., Schauer, T., 2018. Real-time joint axes estimation of the hip and knee joint during gait using inertial sensors. In: Proceedings of the 5th International Workshop on Sensor-Based Activity Recognition and Interaction. In: iWOAR '18.
Nowka, D., Kok, M., Seel, T., 2019. On motions that allow for identification of hinge joint axes from kinematic constraints and 6D IMU data. In: 2019 18th European Control Conference (ECC). pp. 4325–4331.
Olsson, F., Seel, T., Lehmann, D., Halvorsen, K., 2019. Joint axis estimation for fast and slow movements using weighted gyroscope and acceleration constraints. In: 2019 22th International Conference on Information Fusion (FUSION). pp. 1–8.
Pacher, L., Chatellier, C., Vauzelle, R., Fradet, L., 2020. Sensor-to-segment calibration methodologies for lower-body kinematic analysis with inertial sensors: A systematic review. Sensors 20 (11).
Picerno, P., 2017. 25 years of lower limb joint kinematics by using inertial and magnetic sensors: A review of methodological approaches. Gait Posture 51, 239–246.
Picerno, P., Caliandro, P., Iacovelli, C., Simbolotti, C., Crabolu, M., Pani, D., Vannozzi, G., Reale, G., Rossini, P.M., Padua, L., et al., 2019. Upper limb joint kinematics using wearable magnetic and inertial measurement units: an anatomical calibration procedure based on bony landmark identification. Sci. Rep. 9 (1), 1–10.
Picerno, P., Cereatti, A., Cappozzo, A., 2008. Joint kinematics estimate using wearable inertial and magnetic sensing modules. Gait Posture 28 (4), 588–595.
Pinskerova, V., Johal, P., Nakagawa, S., Sosna, A., Williams, A., Gedroyc, W., Freeman, M., 2004. Does the femur roll-back with flexion? J. Bone Joint Surg. Br. Vol. 86 (6), 925–931.
Reinschmidt, C., van den Bogert, A., Lundberg, A., Nigg, B., Murphy, N., Stacoff, A., Stano, A., 1997. Tibiofemoral and tibiocalcaneal motion during walking: external vs. skeletal markers. Gait Posture 6 (2), 98–109.
Sankey, S.P., Robinson, M.A., Vanrenterghem, J., 2020. Whole-body dynamic stability in side cutting: Implications for markers of lower limb injury risk and change of direction performance. J. Biomech. 104, 109711.
Schwartz, M.H., Trost, J.P., Wervey, R.A., 2004. Measurement and management of errors in quantitative gait data. Gait Posture 20 (2), 196–203.
Seel, T., Schauer, T., Raisch, J., 2012. Joint axis and position estimation from inertial measurement data by exploiting kinematic constraints. In: 2012 IEEE International Conference on Control Applications. pp. 45–49.
Tadano, S., Takeda, R., Miyagawa, H., 2013. Three dimensional gait analysis using wearable acceleration and gyro sensors based on quaternion calculations. Sensors 13 (7), 9321–9343.
Vanrenterghem, J., Gormley, D., Robinson, M., Lees, A., 2010. Solutions for representing the whole-body centre of mass in side cutting manoeuvres based on data that is typically available for lower limb kinematics. Gait Posture 31 (4), 517–521.
Victor, J., Van Doninck, D., Labey, L., Innocenti, B., Parizel, P., Bellemans, J., 2009. How precise can bony landmarks be determined on a CT scan of the knee? Knee 16 (5), 358–365.
Vitali, R.V., Perkins, N.C., 2020. Determining anatomical frames via inertial motion capture: A survey of methods. J. Biomech. 106, 109832.
Wada, K., Hamada, D., Tamaki, S., Higashino, K., Fukui, Y., Sairyo, K., 2017. Influence of medial collateral ligament release for internal rotation of tibia in posterior-stabilized total knee arthroplasty: a cadaveric study. J. Arthroplast. 32 (1), 270–273.
Weygers, I., Kok, M., De Vroey, H., Verbeerst, T., Versteyhe, M., Hallez, H., Claeys, K., 2020a. Drift-free inertial sensor-based joint kinematics for long-term arbitrary movements. IEEE Sens. J. 20 (14), 7969–7979.
Weygers, I., Kok, M., Konings, M., Hallez, H., De Vroey, H., Claeys, K., 2020b. Inertial sensor-based lower limb joint kinematics: A methodological systematic review. Sensors 20 (3).
Wilson, D., Feikes, J., Zavatsky, A., O'Connor, J., 2000. The components of passive knee movement are coupled to flexion angle. J. Biomech. 33 (4), 465–473.
Wu, G., Siegler, S., Allard, P., Kirtley, C., Leardini, A., Rosenbaum, D., Whittle, M., D'Lima, D.D., Cristofolini, L., Witte, H., Schmid, O., Stokes, I., 2002. ISB recommendation on definitions of joint coordinate system of various joints for the reporting of human joint motion—part I: ankle, hip, and spine. J. Biomech. 35 (4), 543–548.
Zeng, X., Ma, L., Lin, Z., Huang, W., Huang, Z., Zhang, Y., Mao, C., 2017. Relationship between Kellgren-Lawrence score and 3D kinematic gait analysis of patients with medial knee osteoarthritis using a new gait system. Sci. Rep. 7 (1), 1–8.